

AERODYNAMIC INTERFERENCE BETWEEN OVER-WING-NACELLE AND WING

F. Lange, German Aerospace Center (DLR), Institute of Aerodynamics and Flow Technology,
Lilienthalplatz 7, 38108 Braunschweig, Germany
M. Kotzem, FH Aachen University of Applied Sciences, Bayernallee 11,
52066 Aachen, Germany

Abstract

This paper addresses the complex aerodynamic interaction between a rectangular, unswept wing-segment and an over-the-wing mounted ultra-high bypass ratio (UHBR) engine. In the past, various studies have revealed a beneficial interference effect with respect to installation drag due to over-wing-nacelles (OWN). Previous investigations claimed, that the overall drag of an OWN configuration might be favorable compared to an under-wing-nacelle (UWN) in case of using UHBR engines. Further investigations within the Collaborative Research Center 880 on a short-range aircraft configuration with UHBR OWN engines at $M=0.78$ confirmed a positive installation effect on an OWN. However, the physical mechanism and cause leading to this interference effect could not be identified. Thus, the present investigation is based on a simple test case, allowing for distinct parameter variations to identify the driving mechanism leading to drag reduction on a nacelle located above the wing trailing edge. For that reason, a parameterized rectangular wing was combined with an UHBR engine, taken from the AVACON project. Based on the parameterized wing, several airfoils were investigated ranging from NACA 4-digit series to the NASA SC(2) series. Especially the NACA 4-digit series enables an explicit parameter variation, like airfoil thickness and camber. In addition, flow velocities ranging from $M=0.5$ up to $M=0.8$ were covered to assess transonic effects. Finally, the vertical distance between wing trailing edge and nacelle leading edge was investigated. The evaluation revealed a correlation between lift, induced by the wing, and nacelle drag.

Keywords: UHBR, CFD, OWN, interference effects

1. NOMENCLATURE

AoA	angle of attack
c	mean aerodynamic chord
C_L	lift coefficient
C_D	drag coefficient
c_p	pressure coefficient
d_1	fan diameter
dcts.	drag counts (1 dct. = 0.0001)
H	altitude
lcts.	lift counts (1 lct. = 0.01)
\dot{m}	mass flow
M	Mach number
N	number of grid points
OWN	over-wing-nacelle
p_0	static ambient pressure
p_t	total pressure
p_{t0}	total ambient pressure
Re	Reynolds number

s	wing span
S	distance of stagnation point to symmetry point
T_t	total temperature
T_{t0}	total ambient temperature
UWN	under-wing-nacelle
w	camber
x/c	rel. horizontal distance
z/c	rel. vertical distance
μ	Bypass ratio

2. INTRODUCTION

The increasing efficiency of the latest aircraft, like A320neo or Boeing 737MAX is mainly based on the installation of new engines. These efficient engines are characterized by a high bypass-ratio μ and thus large diameters. Future aircraft aiming for further increasing efficiency are dependent on the progression of the engine manufactures providing ultra-high bypass ratio (UHBR) engines, if the known wing-tube-layout is not significantly changed. However, the integration of UHBR engines below the wing is limited due to the restricted space between wing lower surface and ground. Consequently, alternative engine positions need to be evaluated, which enables the installation of future UHBR engines. A

promising alternative is the installation above the wing trailing edge. There are two famous examples of transport aircraft configurations, which are equipped with an OWN engine, the Fokker VFW-614 and the HondaJet. However, the applied engines feature significantly smaller diameters and the aircraft were operating at subsonic or low transonic speed. For the technology assessment of OWN on large, future transport aircraft, UHBR engines at relevant cruise speeds need to be considered. Previous investigations revealed a complex interference between engine nacelle and wing upper surface. Hooker et al. [1] claimed on the basis of a comprehensive study, that the overall drag of an OWN configuration at $M=0.8$ might be favorable compared to an UWN in case of using UHBR engines. Further investigations within the Collaborative Research Center 880 on a short-range aircraft configuration with UHBR OWN engines at $M=0.78$ confirmed the positive installation effect on an OWN [2]. At the nacelle leading edge around the 6 o'clock position, an increasing suction peak was observed, resulting in beneficial forces in direction of flight. However, the physical mechanism and cause leading to this interference effect could not be identified. Most of the previous studies focused on full aircraft geometries including fuselage, swept and tapered wings leading to complex three-dimensional effects and limited opportunities for explicit parameter variations. Thus, the present investigation is based on a simple test case, allowing for distinct parameter variations to identify the driving mechanism leading to drag reduction on a nacelle located above the wing trailing edge.

3. DEFINITION OF TEST CASE

In order to define a simplified test case for the described investigation, several preliminary studies were performed to attain an accurate flow solution while having specific degrees of freedom to vary the test parameters at the same time. The varied test parameters in this investigation are Mach number M , engine position z/c , airfoil camber w and different airfoil characteristics. These preliminary studies define the geometry dimension, the grid generation strategy and the numerical setup of the test case used in the following investigation.

3.1. Geometry

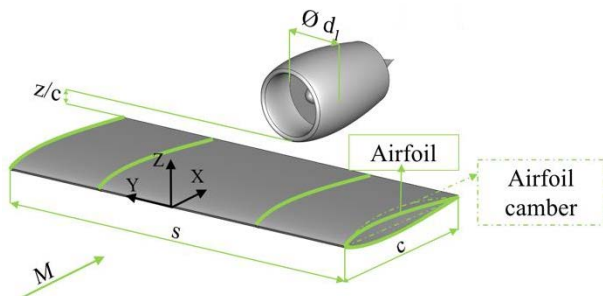


Fig. 1: Test case geometry and parameterization

With the intention of reducing the flow complexity caused by three-dimensional effects, a simplified geometry consisting of an unswept and untwisted rectangular wing

and a representative UHBR engine ($\mu = 16$) placed above the wing trailing edge was developed in CATIA V5 (Fig. 1). To enable geometric changes during the investigation, the wingspan s , the relative vertical distance between wing and nacelle z/c , the mean aerodynamic chord c and the airfoil of the wing were parameterized. In order to eliminate the appearance of wing vortices and therefore reducing the flow complexity thus creating a preferably two-dimensional flow, the wing tips and side walls of the far field are merged. The far field walls at y_{min} and y_{max} feature a symmetry boundary condition to prevent flow reflections back into the control volume. Among others, the influence of this boundary condition is investigated in the preliminary studies.

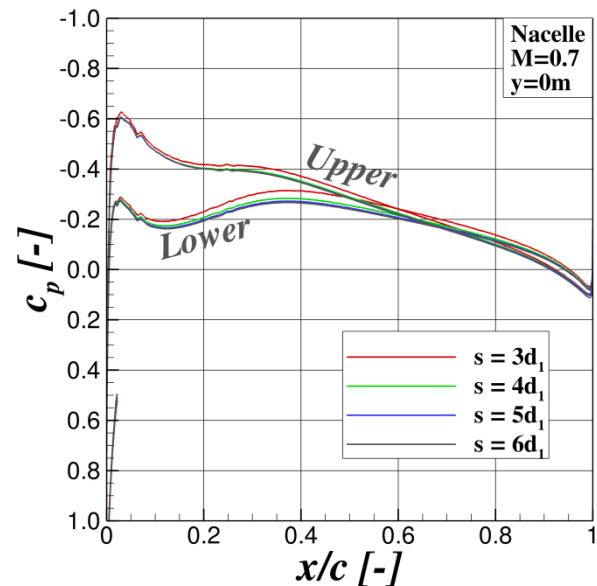
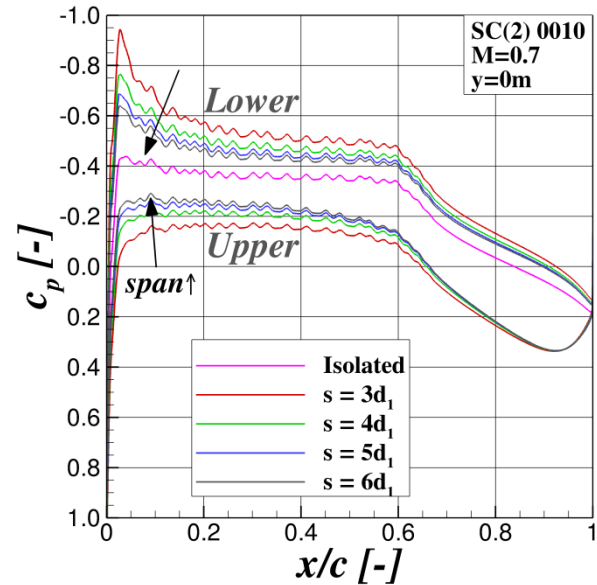


Fig. 2: Pressure distribution of wing (top) and nacelle (bottom) for varying wing span s

Correspondingly, a comparison between the utilization of symmetry walls versus Euler walls for the side walls of the

far field was conducted. The evaluation revealed that both boundary conditions attain the same results. However, the symmetry boundary condition was beneficial with respect to the required simulation time.

To define the wing span s of the test case, the span was systematically increased until no significant changes in the pressure distributions on the wing nor the nacelle were recognizable. In the upper diagram of Fig. 2 the wing pressure distribution is shown in the engine symmetry plane. As can be seen, the pressure distribution converges towards the isolated wing pressure distribution for increased span. Further, the change between each pressure distribution decreases for increasing span values, especially at the rearward part of the wing upper surface. The fluctuations in the pressure distribution are the result of poorly distributed airfoil coordinates, thus affecting the model surface. After the preliminary span study, the airfoils were improved by smoothing and the fluctuations were eliminated.

The lower diagram of Fig. 2 presents the pressure distribution of the nacelle. As seen for the wing, the changes between each pressure distribution become smaller with increasing wing span. There are no significant changes recognizable between a span of $s = 5d_1$ and a span of $s = 6d_1$ at both, the upper and the lower side of the nacelle. The wingspan for the test case was therefore chosen with $s = 6d_1$.

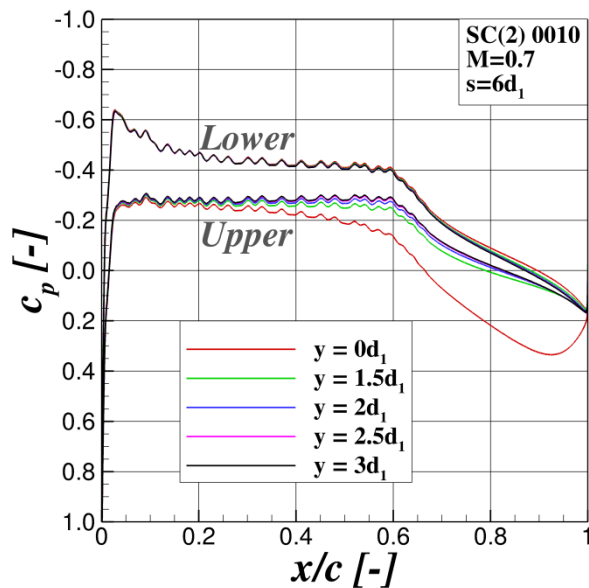


Fig. 3: Spanwise pressure distribution of the wing for a wingspan of $s = 6d_1$

Concerning the later evaluation, the high wing span could show low sensitivity towards changes of the aerodynamic force coefficients of the wing. In order to reduce the evaluation section of the wing, the spanwise pressure distribution of the wing was examined in Fig. 3. It can be observed, that there is no further change of the pressure distribution for a spanwise position of $y > 1.5d_1$ respectively $y < -1.5d_1$. Therefore, only the wing section

from $y = -1.5d_1$ to $y = 1.5d_1$ will be used for the evaluation of aerodynamic force coefficients and comparison of pressure distributions.

3.2. Grid generation strategy

The grid generation was performed with CENTAUR from CentaurSoft [3]. Besides the potential for automation of the grid generation, the software enables the possibility to create a hybrid grid consisting of structured and unstructured grid elements. The grid is made of a surface grid, a prism grid for a more detailed resolution of the boundary layer and a tetrahedral grid which discretizes the remaining volume (Fig. 4). In order to map the viscous sublayer with sufficient accuracy the first layer thickness was chosen according to $y^+ < 1$.

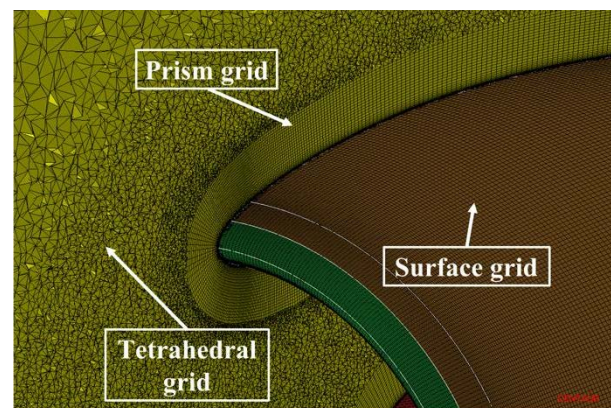


Fig. 4: Grid structure in CENTAUR at the engine inlet

The optimum configuration of the grid was examined in the preliminary studies. Therefore, a grid convergence study and a study concerning the optimum surface grid were performed. In the grid convergence study three different resolution levels (coarse ($N=9'104'154$), medium ($N=23'739'061$), fine ($N=63'571'741$)) were examined to define the necessary settings to obtain a grid independent solution. In Fig. 5 can be seen, that a grid refinement from coarse to medium leads to a change of aerodynamic force coefficients of $\Delta C_L = -0.0354$ lcts. and $\Delta C_D = -3.12$ dcts.. A change from medium to fine leads to a change of $\Delta C_L = -0.0587$ lcts. and $\Delta C_D = -0.27$ dcts.. There are no significant changes between medium and fine grid resolution. Thus, the medium grid resolution was chosen for the upcoming investigation.

Furthermore, the optimum surface grid strategy was investigated. The results of structured, unstructured and hybrid surface grids are compared with each other. The hybrid surface grid is characterized by a structured surface grid on wing, nacelle and engine inlet. The remaining surfaces are discretized with unstructured grid elements. Besides the accuracy of the results, additional criteria were taken into account to determine the chosen surface grid strategy, like the time of grid generation, the effort of grid generation, the adaptability of the grid, the possibility of grid reconstruction and the duration of the simulation. In the end, the hybrid surface grid was chosen since it provides a high accuracy and the opportunity for grid

reconstruction of the most important model surfaces. Concurrently, this approach requires moderate time and effort during grid generation and short simulation duration.

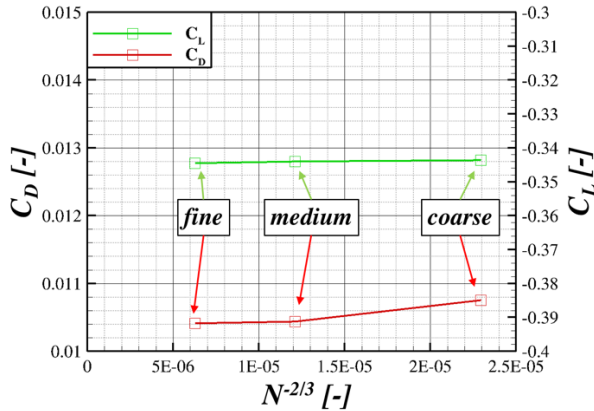


Fig. 5: Change of C_L and C_D for different grid resolutions

3.3. Numerical setup

For the numerical fluid dynamic calculations, the DLR TAU code [4] was utilized. This solver is based on a finite-volume approach to solve the compressible Reynolds-averaged Navier-Stokes (RANS) equations. The space discretization is done by a central scheme with artificial dissipation and combined with the LU-SGS scheme for time stepping. The backward Euler method was used as relaxation solver. Turbulence effects were modelled with the SSG/LRR- $\ln\omega$ model [5], [6] since it provides an improved flow solution accuracy in comparison to one- or two-equation model approaches and at the same time stable convergence behavior. For fast convergence, the multigrid technique was used.

Alt.	M	Bypass outlet			Core outlet		
		p/p_0	T_e/T_0	\dot{m}	p/p_0	T_e/T_0	\dot{m}
[10 ³ ft]	-	[-]	[-]	$\frac{\text{kg}}{\text{s}}$	[-]	[-]	$\frac{\text{kg}}{\text{s}}$
20	0.5	1.3	1.03	462.9	1.08	2.27	19.6
25.5	0.6	1.45	1.04	447.8	1.15	2.29	20.5
30	0.7	1.63	1.05	435.2	1.24	2.3	22.1
34	0.8	1.87	1.07	420.5	1.39	2.33	23.7

The engine used in this study was previously developed and already utilized in the AVACON investigations [7]. In the current investigation the engine model is powered and produces a thrust force for a representative modern mid-range aircraft for the given Mach numbers (Tab. 1). To

ensure a constant Reynolds number for every examination point, the atmospheric conditions and therefore the altitude was adapted accordingly to each Mach number and its specific thrust setting. The thrust setting of the utilized UHBR engine is controlled by pressure ratio and temperature ratio. The mass flow at bypass and core outlet was monitored as control parameter. The outlet surfaces are coupled with the engine inlet to determine the inlet flow which has to be in balance with the outlet flow. In Tab. 1 the most important values concerning the used engine parameters are presented. Losses at the engine inlet or losses caused by the thermodynamic processes are already taken into account.

4. PARAMETER VARIATION

The prescribed test case enabled a distinct parameter variation to identify basic interference effects between nacelle and wing. The airfoil shape and engine position were varied systematically throughout this study. Moreover, the Mach number range between $M=0.5$ up to $M=0.8$ was investigated to identify the impact of transonic effects. Besides the various wing/engine configurations, each component was simulated stand-alone at identical reference conditions to assess the interference effect. In addition should be noted, that all simulations were accomplished at an angle of attack of $\text{AoA}=0^\circ$, to exclude additional effects by diverging incidence angle. Moreover, the provided engine settings guaranteed almost identical stagnation lines on the isolated nacelle leading edge, independent from the chosen Mach number. The evaluation of aerodynamic coefficients is based on a central wing segment with a representative area and the nacelle outer surface, which is defined from the stagnation line at the engine highlight up to the nacelle trailing edge. The interference drag is defined by the difference between the coefficients for the installed and isolated geometry at identical reference conditions. Furthermore, the pre-entry and post-exit thrust corrections were considered as part of the drag-thrust bookkeeping.

First, the general impact of the OWN installation on wing and nacelle will be presented on the basis of pressure distributions in the engine symmetry plane for a representative configuration. Fig. 6 compares the pressure distribution on nacelle and wing (red) with results from isolated simulations (black). Note, the isolated pressure distributions are identical for upper and lower surface, because the geometry is symmetrical and investigated at $\text{AoA}=0^\circ$. The upper plot in Fig. 6 compares the pressure distributions on the outer nacelle surface, since this section is relevant for the aerodynamic coefficients and thus the source for the interference effects, which should be examined. The pressure distribution for the installed engine reveals a distinct variation along the first half of the lower nacelle surface in comparison with the isolated nacelle. This is caused by the presence of the wing and the close coupling of the two components. The leading edge pressure peak drops by about 0.5. In contrast, the upper nacelle surface experiences a minimal variation compared to the isolated pressure distribution. The absolute pressure level increases slightly along the chord; however the

general trend is identical. This observation suggests that the upper end of the nacelle is less affected by the wing, but experiences a reduction of the local effective angle of attack α_{eff} .

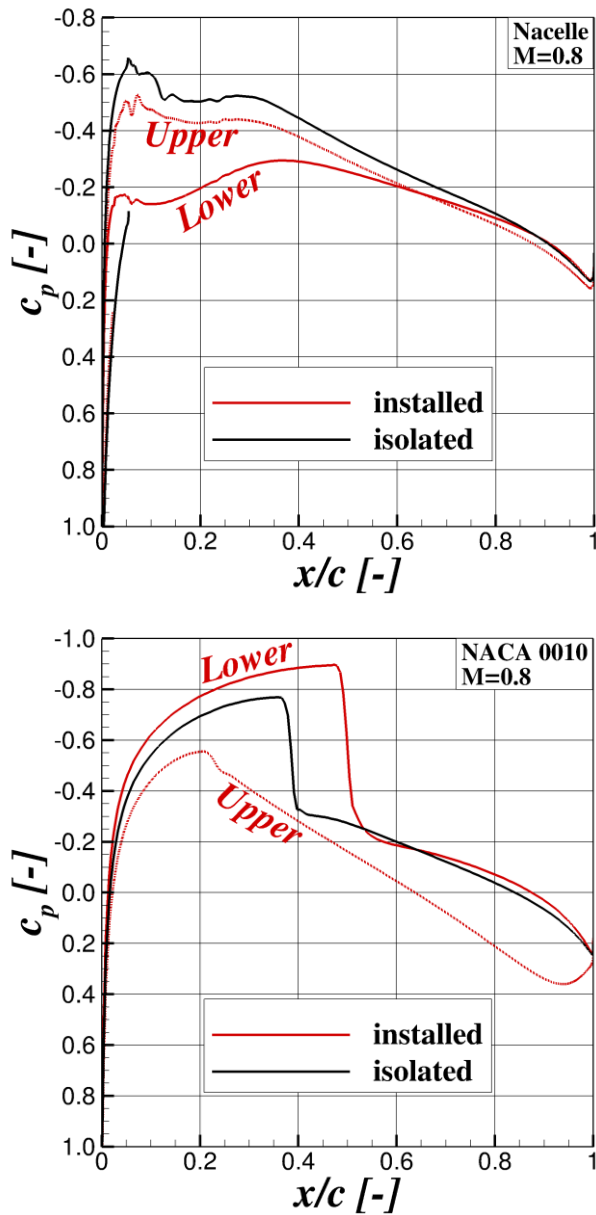


Fig. 6: Basic installation effects of OWN

The plot at the bottom of Fig. 6 presents the results for the wing section in the engine symmetry plane. Based on this illustration, a significant difference between installed and isolated pressure distributions can be noted. The c_p -distribution for the lower wing reveals a decreasing pressure level and downstream shift of the shock location by $\Delta x/c \approx 0.1$. The c_p -trend over the last 50% chord is almost identical with the isolated result. In contrast, the entire c_p -distribution on the upper wing surface is affected by the OWN. The pressure distribution is characterized by an upstream shift of the suction peak and increasing c_p -level up to the wing trailing edge. Thus can be stated, that the OWN installation has an impact on the upper wing pressure level affecting the whole wing chord. Furthermore, a

decreasing effective angle of attack α_{eff} is induced by the OWN installation resulting in flow accelerations on the lower wing surface.

4.1. Engine position

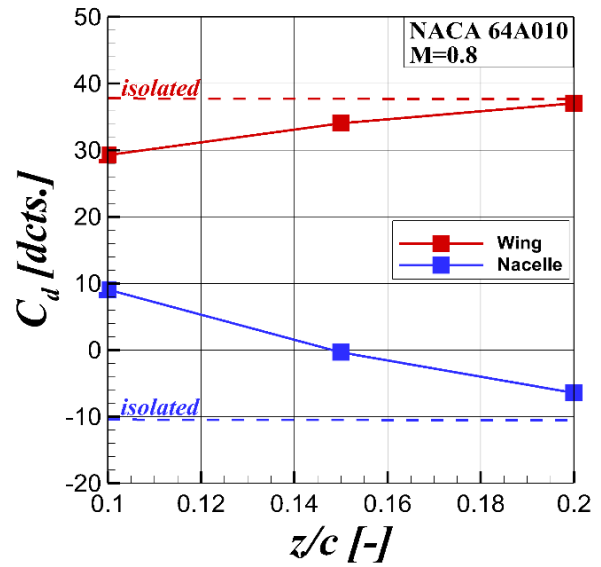


Fig. 7: Drag coefficients on nacelle and wing dependent on vertical engine position

At the beginning of the parameter variation, the impact of the vertical distance between nacelle and wing will be evaluated. Therefore, the airfoil NACA 64A010 was chosen at $M=0.8$, while the vertical engine position was varied between $z/c=0.1 \dots 0.2$. The resulting drag coefficients are plotted in Fig. 7.

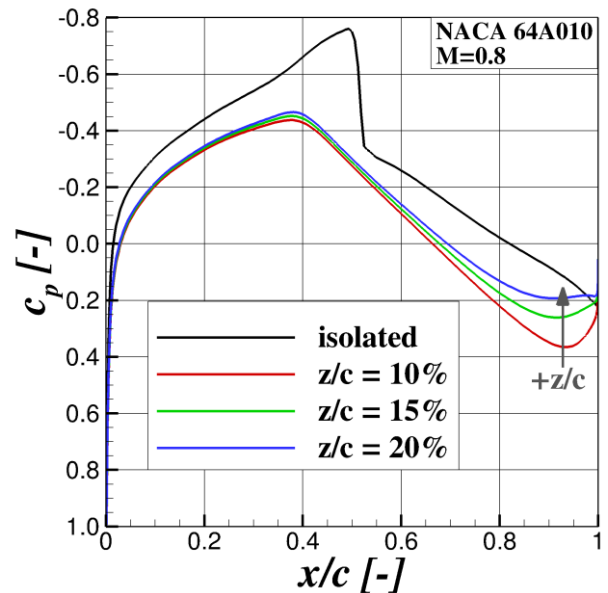


Fig. 8: c_p -distribution on upper wing with respect to a varying vertical distance between nacelle and wing

Based on this plot can be stated, that the drag coefficients of the installed components converge towards the result for the isolated components with increasing vertical distance. Nevertheless, a visualization of the pressure distributions along the upper wing in Fig. 8, reveals a clear impact due to the presence of the OWN for all installed configurations. Although, the drag coefficient persuades a convergence towards the isolated wing characteristic, the pressure distribution reveals a clear impact of the OWN and all installed configurations deviates from the isolated c_p -distribution. The minimum c_p for all installed configuration is located at a similar chordwise position of 0.4. In addition, the first 70% chord features almost no variation as a result of the engine displacement. Solely, a decreasing pressure level with increasing vertical distance can be observed at the wing trailing edge.

Consequently, the presence of the UHBR engine is determining the aerodynamics on the upper wing, independent from the vertical engine position. The lower wing is blanked out due to minor changes over the parameter variation.

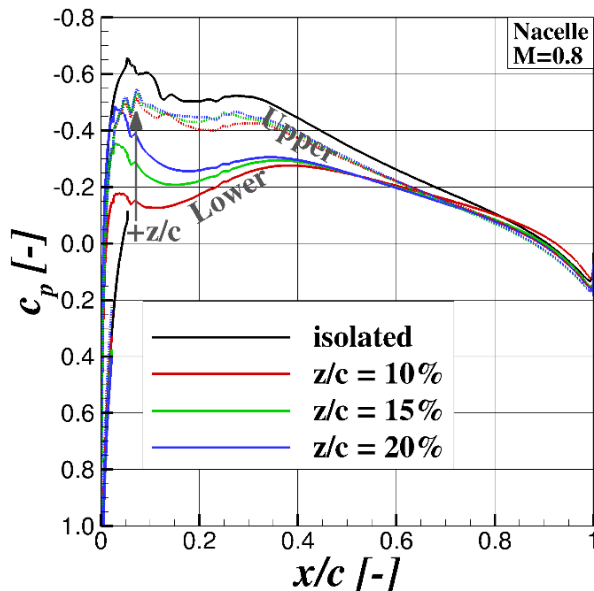


Fig. 9: c_p -distributions in nacelle symmetry with respect to a varying vertical distance between nacelle and wing

By evaluating the c_p -distributions on the nacelle in Fig. 9, a distinct variation on the lower surface pressure distribution can be noted, whereas the upper surface features small fluctuations. In contrast to the wing, a convergence towards a symmetrical flow around the nacelle can be assumed. The c_p -level on the lower nacelle decreases with increasing vertical distance, whereby the difference between upper and lower c_p -distribution decreases. Nevertheless, the beneficial installation effect on the nacelle, which is the reason for this investigation, could not be observed yet. All nacelle drag coefficients of the installed engine are above the results of the isolated nacelle.

4.2. Camber line variation

The utilization of the NACA 4-digit series enabled an explicit variation of the camber line to investigate the impact of varying lift coefficients induced by the upstream located wing on the OWN. Therefore, the NACA 0010, 1510, 2510 and 3510 were investigated for a constant engine position of $z/c=0.15$ at $M=0.8$. First, the results for the isolated and installed wing depending on the wing camber will be presented with focus on the lift coefficient. An overview is given in Fig. 10. In general, the wing lift coefficient is increasing with increasing camber. The lift coefficients for the installed configuration are always lower than for the isolated configuration at identical wing camber. The offset between $w=0\% \dots 2\%$ is almost constant, which supports the assumption of a reduced effective angle of attack due to the OWN. However, the trend for the isolated wing drops between 2% and 3%, resulting in a minimal lift gain due to a further increasing camber, whereas the installed wing features a further increasing lift coefficient for $w=3\%$, reaching almost the level of the isolated wing.

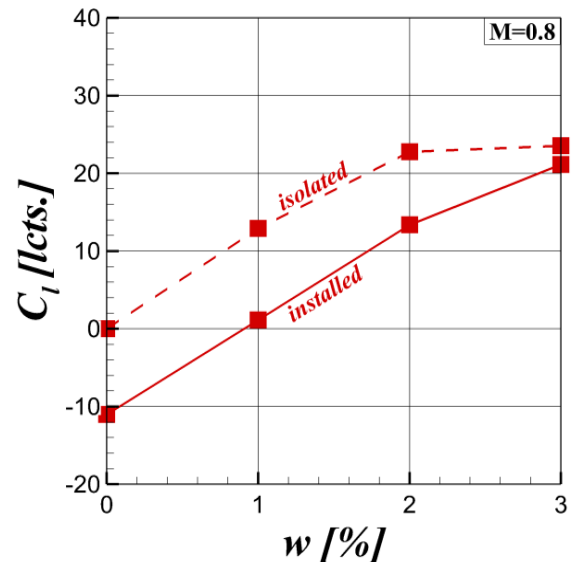


Fig. 10: Wing lift coefficient dependent on camber for isolated and installed wing

An evaluation of the pressure distributions suggests, that the aerodynamic limit of this airfoil at $M=0.8$ is reached and that neither the c_p -level nor the chordwise shock position can be increased to generate more lift. In contrast, the installed wing experiences an upstream shift and c_p -level increase due to the presence of the OWN. Accordingly, the airfoil has to counteract the presence of the engine before reaching the aerodynamic limits of the airfoil. Consequently, the lift coefficients for the isolated and installed wing are almost identical for $w=3\%$ despite the offset for the less cambered airfoils. As a consequence, the camber line variation provides a broad lift range for the installed configuration to assess the impact on the nacelle. A first overview is provided in Fig. 11, presenting the drag coefficients of the nacelle for the installed engine

dependent on the camber line variation. As reference, the drag coefficient of about -10 dcts. for the isolated engine is highlighted as dashed line. This plot reveals a decreasing nacelle drag with increasing wing camber. Already for $w=2\%$ the installed nacelle features positive interference drag. The linear trend describes a drag reduction of nearly 25 dcts. between the minimum and maximum camber. At $w=3\%$ a drag benefit of about 12 dcts. can be found in comparison with the isolated nacelle.

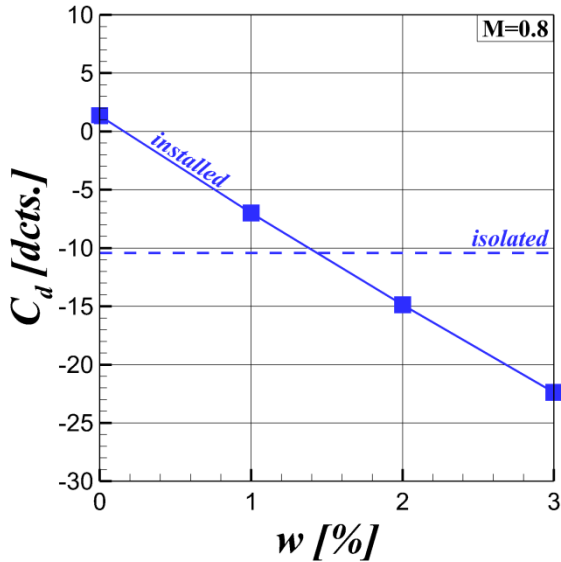


Fig. 11: Nacelle drag coefficient dependent on wing camber

Concurrently, the nacelle lift coefficient is almost identical for all configurations. Consequently, a correlation was found between the lift, induced by the wing, and nacelle drag. However, the physical reason for this beneficial interference effect on the nacelle is not described yet. Therefore, in a first step the pressure distributions on the nacelle for $w=0\%$ and $w=2\%$ are compared in Fig. 12. The pressure distributions extracted on the upper surface are indicated by a dashed line, the lower surface by solid lines. On the upper surface, the principal shape of the pressure distribution is similar. Due to the wing camber, the suction peak on the upper surface is less pronounced. Instead, the c_p -level further downstream the nacelle decreases by $\Delta c_p < 0.1$. The changes of the lower nacelle pressure distribution are limited to the first 30% chord. Resulting from the airfoil camber, a strong suction peak develops at the nacelle leading edge. This low pressure region is located on the curved and forward facing nacelle leading edge. Thus, the resulting force component is oriented in direction of flight. Consequently, the pressure drag component decreases. This pronounced suction peak corresponds with previous observations on the CRC 880 REF3-configuration. Nevertheless, the physical cause for this suction peak needs to be found. Since the suction peak around curved leading edges depends among others on the stagnation line, the position of the stagnation point was evaluated for the lower and upper nacelle section for all four camber variations.

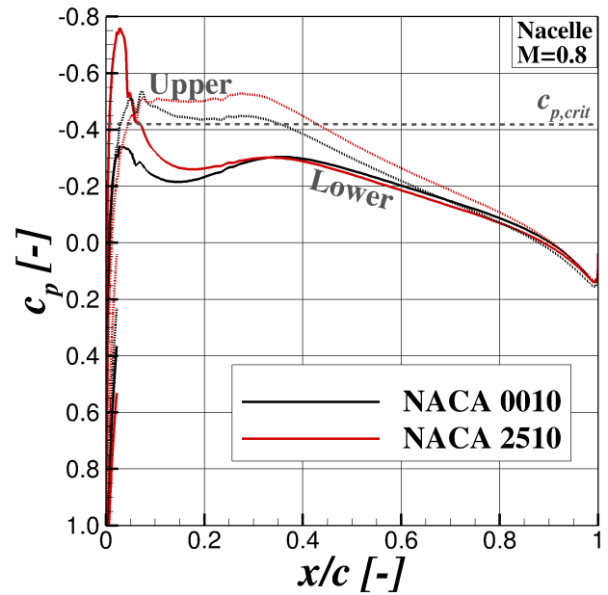


Fig. 12: c_p -distribution on nacelle showing the impact of wing camber

The result is presented in Fig. 13. This plot reveals an uneven displacement of the stagnation line between upper and lower section with increasing wing camber. The stagnation line at the lower section moves with increasing wing camber into the engine inlet.

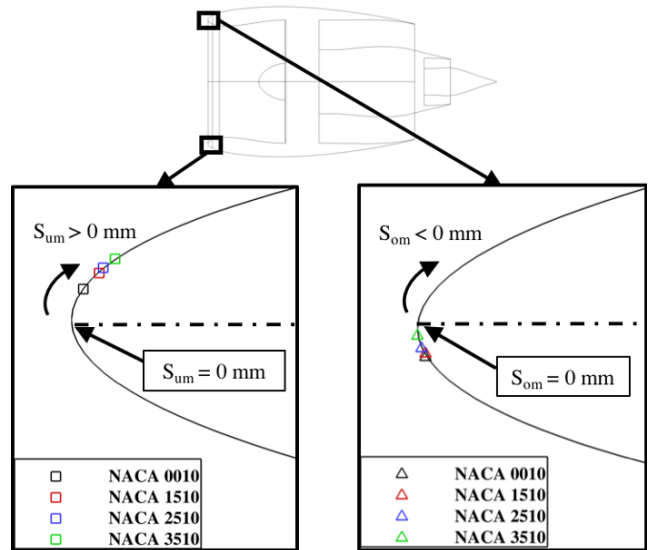


Fig. 13: Stagnation line displacement on lower and upper nacelle section dependent on wing camber

Consequently, the flow acceleration around the nacelle leading edge increases. Whereas, the comparative small stagnation point displacement on the upper nacelle surface results in a reduction of the corresponding suction peak. Consequently, the uneven movement of the stagnation line results in an asymmetric development of the suction peaks, whereas the increase of the lower suction peak is larger than the upper suction peak decrease. Thus, an increasing beneficial pressure force component can be found on the

nacelle. The reason for this asymmetric stagnation line movement can be found by evaluating the downwash induced by the wing.

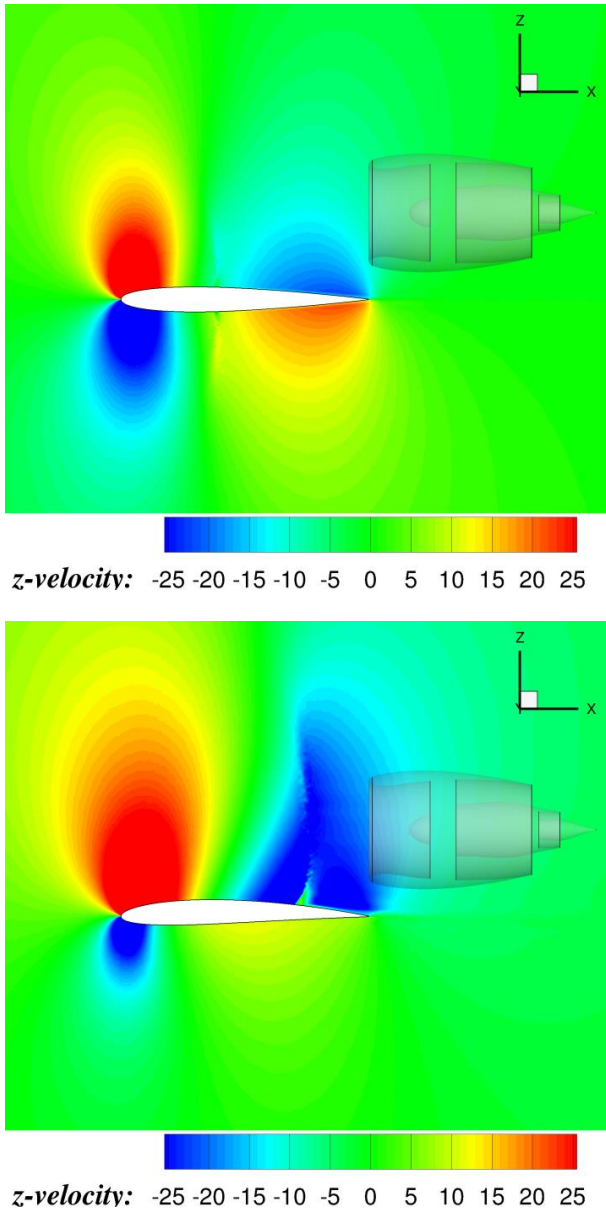


Fig. 14: Comparison of z-velocities induced by symmetrical and cambered airfoil

Fig. 14 compares the z-velocities induced by the isolated symmetrical NACA 0010 and cambered NACA 2510. The engine rendering serves as orientation. Based on this illustration, a pronounced downwash can be identified above the rear part of the cambered airfoil in comparison with the symmetrical airfoil. This downwash interacts with the OVN and induces a negative local incidence resulting in a stagnation line movement. Due to the large inlet diameter of the OVN, the upper section experiences a smaller downwash than the lower section. For that reason, the stagnation line movement is less pronounced on the upper nacelle section. Based on this observations can be assumed, that the downwash, which depends on the lift induced by the wing, leads to an asymmetrical stagnation

line movement on the nacelle leading edge. This in turn causes an uneven development of the suction peak on lower and upper nacelle section, resulting in a beneficial pressure force in the direction of flight.

4.3. Mach number variation

Finally, a variation of the Mach number for a configuration featuring the beneficial nacelle interference was performed. Therefore, the configuration with the NACA 2510 was investigated at four Mach numbers between 0.5 and 0.8. The variation of the nacelle drag component over the Mach number is presented in Fig. 15.

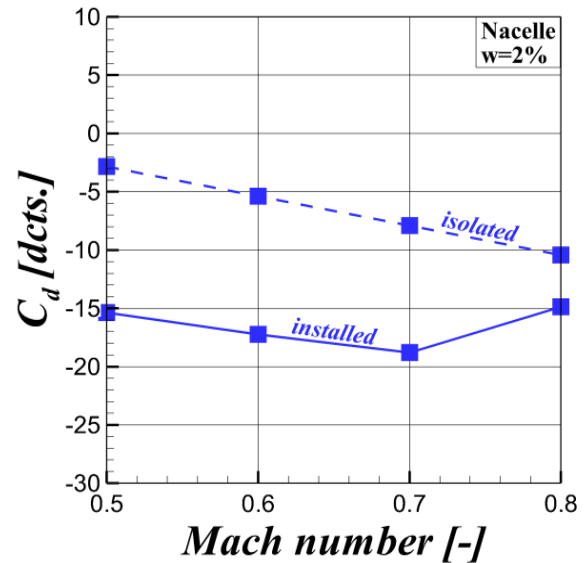


Fig. 15: Nacelle drag coefficient in the presence of the NACA 2510 over Mach number for isolated and installed nacelle

This plot summarizes the results for the isolated and installed nacelle at AoA=0°. In general, the drag coefficient for the installed nacelle is always below the isolated reference at each Mach number. Between M=0.5 and M=0.7, the curves for isolated and installed nacelle are almost in parallel and thus the drag difference constant. The results for the isolated nacelle reveal a linear trend between increasing Mach number and decreasing drag coefficient. In contrast, the positive trend for the installed nacelle deviates for M=0.8. Nevertheless can be stated, that this interference effect between wing and OVN can be observed for both subsonic and transonic flow conditions.

5. EVALUATION OF GENERAL FINDINGS WITHIN PARAMETERSPACE

The presented parameter variations show a high complexity between wing upper surface and engine nacelle of an OVN configuration. Both components influence the flow causing positive and negative effects concerning their aerodynamic efficiency. A physical explanation for the mentioned positive interference effect could be stated after the variation of the camber line. The interference effect is based on the stagnation line movement at nacelle leading

edge. This movement is highly dependent from the downwash of the wing and therefore highly influenceable by the wing induced lift. A stronger downwash leads to a higher z -velocity component at the wing trailing edge, thus influencing the local incidence angle at the nacelle leading edge. This causes an uneven stagnation line movement, which leads to an intensified suction peak at the nacelle lower side and a decreased suction peak on the upper side. Because of the larger movement on the lower side and the surface curvature, the resulting pressure force inhibits a component pointing in flight direction hence reducing the drag of the nacelle.

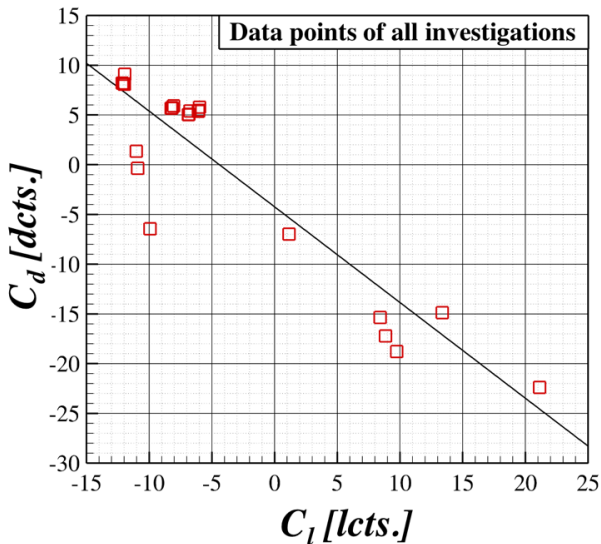


Fig. 16: Dependence of the nacelle drag towards the lift induced by the wing

The physical explanation addressing the occurrence of the positive interference effect is based on the findings from the camber line variation. Since there are only four simulations in this parameter variation, the consistency of the expressed explanation has to be verified by all gathered data points out of all parameter variations. For this purpose, Fig. 16 exhibits the nacelle drag versus the lift produced by the wing for all gathered data points. A trend supporting the given explanation can be recognized. The increase of wing lift and therefore an increase of the downwash velocity, results in decreased drag values for the nacelle. Only one data point ($C_l \approx -10$ lcts. and $C_d \approx -6.5$ dcts.) deviates significantly from this trend. This can be explained by the findings from chapter 4.1. At this data point, a maximum distance of $z/c = 0.2$ is examined during the parameter variation of the engine position. As seen before, a convergence towards a symmetrical flow around the nacelle can be assumed for increasing z/c , hence the nacelle is less affected by the stated interference effect. Further, a cross check was performed with the purpose to examine whether the positive interference effect is dependent from the lift of the wing or solely driven by the downwash. Therefore an additional symmetrical airfoil with higher thickness ratio was investigated and compared to the results of the previously used NACA 0010. As can be seen in Fig. 17, the increased thickness ratio causes an

intensified downwash while the lift of the wing remains the same at $C_l = 0.0$ for the isolated case. The result for the installed case reveals a drag reduction on the nacelle by $\Delta C_d = -4.63$ dcts. for the thicker airfoil and an intensified suction peak on the lower side of the nacelle was observed. This indicates that the occurrence of the positive interference effect is not dependent, yet highly influenceable, by the lift of the wing.

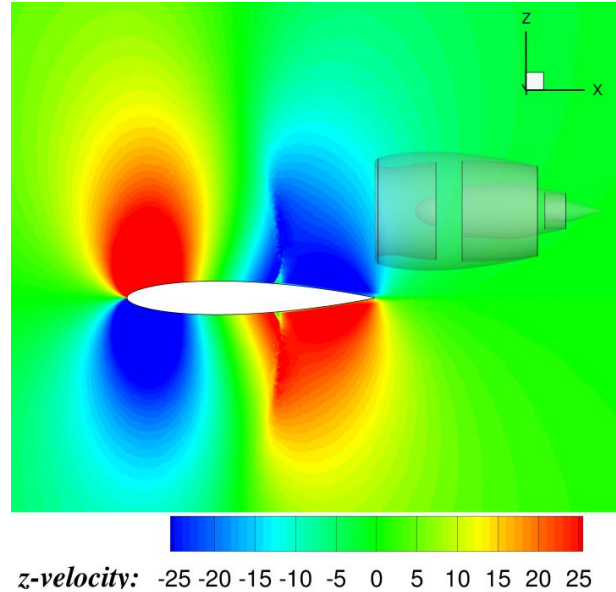


Fig. 17: z -velocities induced by a higher thickness ratio of a symmetrical airfoil

As mentioned before, an important aspect for the existence of the beneficial pressure force is the uneven stagnation line movement between the nacelle upper and lower side.

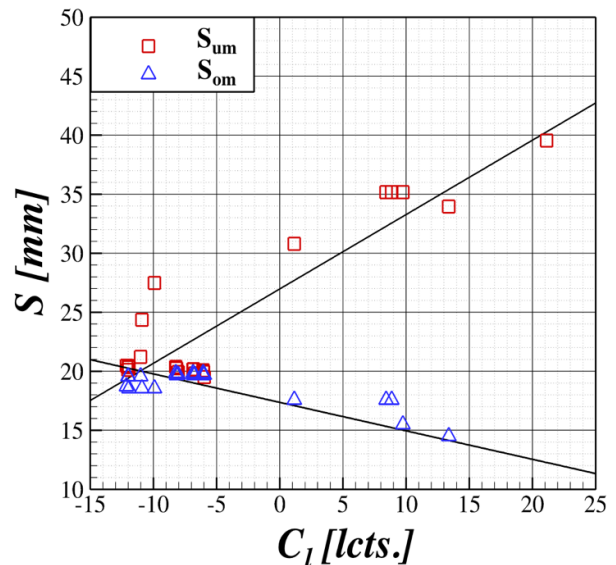


Fig. 18: Stagnation line movement for upper and lower side of the nacelle in dependency of the wing lift at all investigated data points

The stagnation line at the lower side moves inside the engine while the stagnation line at the upper side moves outside the engine. Due to the uneven movement the increase of the lower suction peak is larger than the upper suction peak decrease, hence a beneficial pressure force in flight direction occurs. As well as for the nacelle drag, this statement has to be verified by reviewing all data points. The stagnation line movement for upper (S_{om}) and lower (S_{um}) side of the nacelle versus wing lift can be seen in Fig. 18. S expresses the distance between the symmetry point of the nacelle leading edge and the stagnation point in the engine symmetry plane. The movement of S inside the engine is associated with an increasing value, while an outside movement results in a decrease. The figure exhibits, as assumed, a stagnation line movement on the lower side with a positive gradient for increased lift values, while the upper side indicates a negative gradient. Compared with each other, the gradients underline the uneven movement throughout the whole parameter variations. The trend line for the lower stagnation line is much steeper than for the upper side, thus explaining why a beneficial pressure force is generated.

6. CONCLUSION

The presented investigation addresses the physical explanation for the positive interference effect on the engine nacelle for an OWN, which was examined in previous studies. These studies observed an increased suction peak at the nacelle leading edge around the 6 o'clock position, resulting in beneficial forces in direction of flight. In order to identify the reason for this beneficial force, a simplified test case was developed. This test case enabled a systematic parameter variation to identify interference effects between wing and nacelle. Therefore, the RANS-equations were solved with the DLR TAU code. Besides geometrical changes of the airfoil and the engine position, also the Mach number was varied. The key results of this investigation concerning the complex interference between wing and engine nacelle can be summarized as follows:

First, general installation effects were observed for an OWN placed at the wing trailing edge with symmetrical airfoils. The installation causes a decreased pressure level and a downstream shift of the shock location on the wing lower side, whereas the pressure level on the wing upper side is increased and the shock is shifted upstream. Furthermore, the suction peak at the leading edge of the nacelle dropped on the upper and lower side, whereby the change at the lower side was significantly higher. The variation of the engine position revealed a convergence towards a symmetrical flow around the nacelle. Concurrently the aerodynamics on the upper wing surface are determined by the presence of the UHBR engine. Due to the variation of the camber line, the stagnation line movement at the nacelle leading edge could be identified as the leading mechanism for the appearance of the positive interference effect on the nacelle. The downwash of the wing is distinguished to be the main driver for the stagnation line movement which leads to the mentioned suction peak at the nacelle leading edge 6 o'clock position.

Finally, the positive interference effect was discovered at subsonic as well as at transonic Mach numbers. The gathered knowledge of this investigation can be used as a foundation for upcoming research projects concerning the complex interference effects of an OWN. Besides the potential benefit of the analyzed interference effect, several other findings cannot be neglected. It has to be mentioned, that a shock wave occurring on the wing upper surface at transonic Mach numbers can significantly influence the flow towards the engine. The impact of such a disturbed flow towards the engine inlet can have serious negative consequences, such as flow separation at the fan or compressor. This potential impact was not covered in this investigation, but it has to be handled and analyzed in upcoming investigations to evaluate the full potential of an OWN configuration.

7. ACKNOWLEDGEMENT

The authors would like to thank Julian Bijewitz from MTU Aero Engines for the valuable exchange and the provision of engine data and Constance Heykena from the Technical University Braunschweig for providing the engine geometry.

8. REFERENCES

- [1] Hooker, J., Wick, A., Zeune, C., Agelastos, A.: Over-the-Wing Nacelles Installations for Improved Energy Efficiency, 31st AIAA Applied Aerodynamics Conference, San Diego, CA (2013)
- [2] Lange, F., Rudnik, R.: Aerodynamic Optimization of the OWN Configurations REF3 and REF4 in Cruise Flight, Fundamentals of High Lift for Future Civil Aircraft, Springer (2020)
- [3] CentaurSoft: Online CENTAUR Manual, <https://www.centaursoft.com/centaur-manual>
- [4] Institute of Aerodynamics and Flow Technology (Deutsches Zentrum für Luft- und Raumfahrt e.V.): Technical Documentation of the DLR TAU-code Release 2019.1.0, Technical Report
- [5] Eisfeld, B., Brodersen, O.: Advanced Turbulence Modelling and Stress Analysis for the DLR-F6 Configuration, 23rd AIAA Applied Aerodynamics Conference, Toronto (2005)
- [6] Eisfeld, B., Togiti, V., Braun, S., Stürmer, A.: Reynolds-Stress Model Computations of the NASA Juncture Flow Experiment, AIAA SciTech 2020 Forum, Orlando (2020)
- [7] Wöhler, S.; Hartmann, J.; et al.: Preliminary Aircraft Design for a Midrange Reference Aircraft taking Advanced Technologies into Account as Part of the AVACON Project for an Entry into Service in 2028. Deutsche Gesellschaft für Luft- und Raumfahrt - Lilienthal-Oberth e.V. (2019) <https://doi.org/10.25967/480224>.